

AION: Aerial Indoor Object-Goal Navigation Using Dual-Policy Reinforcement Learning

Zichen Yan, Yuchen Hou, Shenao Wang, Yichao Gao, Rui Huang, Lin Zhao

Abstract—Object-Goal Navigation (ObjectNav) requires an agent to autonomously explore an unknown environment and navigate toward target objects specified by a semantic label. While prior work has primarily studied zero-shot ObjectNav under 2D locomotion, extending it to aerial platforms with 3D locomotion capability remains underexplored. Aerial robots offer superior maneuverability and search efficiency, but they also introduce new challenges in spatial perception, dynamic control, and safety assurance. In this paper, we propose AION for vision-based aerial ObjectNav without relying on external localization or global maps. AION is an end-to-end dual-policy reinforcement learning (RL) framework that decouples exploration and goal-reaching behaviors into two specialized policies. We evaluate AION on the AI2-THOR benchmark and further assess its real-time performance in IsaacSim using high-fidelity drone models. Experimental results show that AION achieves superior performance across comprehensive evaluation metrics in exploration, navigation efficiency, and safety. The video can be found at <https://youtu.be/TgsUm6bb7zg>.

I. INTRODUCTION

Enabling robots to find objects specified by text instructions is a fundamental capability for embodied AI. As a branch of embodied navigation, ObjectNav has attracted widespread attention and holds significant practical value across a wide range of applications, including service robots, disaster rescue, and autonomous inspection. This task can be decomposed into two stages: exploration before the target is observed and goal-reaching after target detection.

Indoor ObjectNav has been well developed on ground robots. Nevertheless, they typically rely on global localization and semantic maps for exploration [1]. Given such maps, large language models (LLMs) demonstrate a strong potential for ObjectNav by enabling high-level scene reasoning and subgoal selection [2]–[4]. However, indoor localization and mapping are prone to accumulated errors and can become unreliable in purely visual servoing systems. To avoid these issues and simplify manual fine-tuning across multiple conventional, end-to-end methods [5]–[9] have emerged as a promising direction by directly inferring actions from multimodal observations.

In the aforementioned methods, agents are restricted to 2D locomotion with cameras typically mounted at a fixed altitude, making it difficult to search cluttered environments and find objects at different height levels. In contrast, aerial robots provide greater flexibility through 3D motion, allowing them to fly over obstacles and gain a broader aerial

The authors are with the Department of Electrical and Computer Engineering, National University of Singapore, Singapore. Email: zichenyan@u.nus.edu, zhaolin@nus.edu.sg

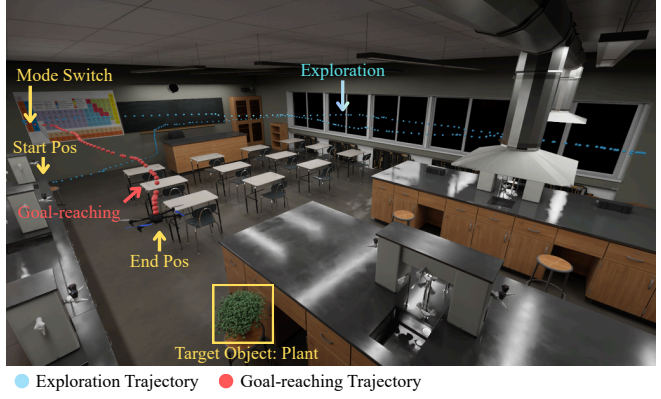


Fig. 1. Demonstration of two-stage aerial ObjectNav with policy switching between exploration (AION-e) and goal-reaching (AION-g).

view. However, the expanded locomotion space also introduces new challenges. For RL policies, the 3D action space significantly increases training complexity and poses higher demands on spatial perception. Moreover, indoor map-based methods rely on accurate global poses and incur high 3D computational costs. Beyond perception and localization, drone navigation is prone to collisions in cluttered scenes, which is often overlooked by prior works. Many algorithms are evaluated only in Habitat [10] or AI2THOR [11], where motion execution is simplified by teleportation instead of dynamic control. The real-time performance and navigation safety under realistic robot dynamics remain unexplored.

In this paper, we present **AION** (Aerial Indoor Object-Goal Navigation), an end-to-end dual-policy RL framework designed to support 3D ObjectNav. As is shown in Fig. 1, AION consists of two policies: AION-e for exploration, and AION-g for goal-reaching. The navigation performance is thoroughly evaluated on both the AI2THOR benchmark and the IsaacSim platform that simulates realistic physical dynamics. Our main contributions are as follows:

- We extend indoor zero-shot ObjectNav from 2D to 3D locomotion. A dual-policy strategy is proposed to improve mapless exploration and goal-oriented navigation using RGB-D images, textual object classes, and altitude measurement.
- Beyond improving benchmark metrics, AION emphasizes real-time performance and safety during aerial navigation, which is validated in IsaacSim under realistic drone dynamics.

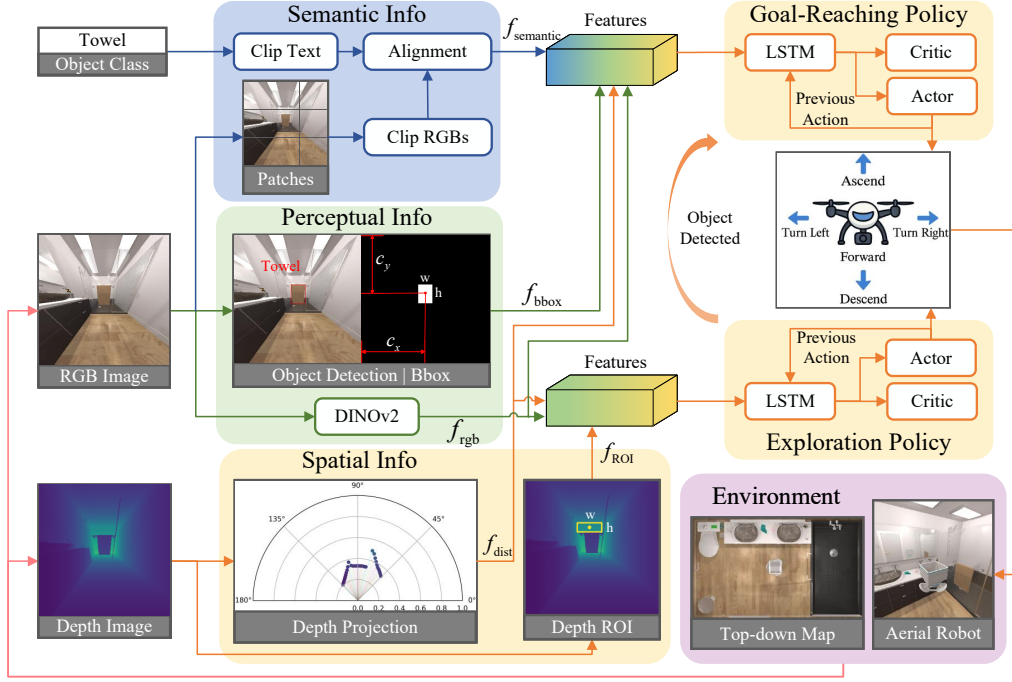


Fig. 2. Overview of the proposed dual-policy RL framework for aerial indoor ObjectNav.

II. RELATED WORKS

A. Zero-Shot ObjectNav

When perception and localization are fully known and accurate, modular methods have proven to be a mature solution for 2D zero-shot ObjectNav [1], which typically combines high-level planning and low-level goal-reaching while maintaining a semantic map for exploration. To accelerate the search, subgoal selection can be improved by rule-based methods [12], foundation models [13], RL policies [14], or powerful LLMs [3], [4]. For pure visual servoing systems that lack LiDAR sensors, map-based methods are prone to unreliable indoor localization. To address this problem, Cai [15] explored mapless ObjectNav through scene reasoning by LLMs.

Without explicit mapping, end-to-end methods aim to infer actions directly from multi-modal observations, or integrate latent localization and mapping into the planner [16]. Existing end-to-end methods focus on studying object relationship graphs [5], [6], object-goal attention [9], [17], and memory mechanisms [18]. To achieve zero-shot generalization, foundation models [19], [20] are utilized for vision-language grounding, allowing the agent to find novel object categories without requiring object-specific finetuning. The work similar to ours is DAT [21] that adaptively fuses search and navigation for 2D ObjectNav.

B. Aerial ObjectNav on Drones

Existing aerial ObjectNav research is largely explored under the vision-language navigation (VLN) paradigm, particularly in outdoor environments [22]–[25]. Liu [26] extended aerial VLN to indoor scenarios but ignores flight dynamics and safety. In addition, Huang [27] achieved efficient indoor ObjectNav on both ground and aerial robots but in known

environments with a pre-built global map. The nature of VLN on drones lies in grounding language and vision to follow human instructions. However, VLN struggles to explore the environment when prebuilt maps or detailed textual guidance are unavailable. Therefore, aerial VLN methods do not apply to classical ObjectNav tasks when only the target object class is specified. So far, 3D ObjectNav in indoor environments remains largely unresolved, and we focus on end-to-end vision-based solutions to avoid dependence on perfect pose estimation and pre-built maps.

III. PROPOSED METHODS

As illustrated in Fig. 2, the proposed framework employs an exploration policy AION-e while the object is undetected and switches to a goal-reaching policy AION-g once the object is detected. AION-e and AION-g adopt the same model architecture and use a partially shared set of multi-modal features. Unlike prior ObjectNav methods, we incorporate depth information into the end-to-end pipeline to enhance spatial understanding, enabling the agent to learn obstacle avoidance and efficient 3D navigation in cluttered environments.

A. Task Definition

In an aerial ObjectNav task, the agent is supposed to find the target object c_t from a class set C . The observations consist of an RGB image $\mathcal{I}_{\text{rgb}} \in \mathbb{R}^{H \times W \times 3}$, a depth image $\mathcal{I}_{\text{depth}} \in \mathbb{R}^{H \times W}$, a target object class c_t and the current altitude H . The action space is extended to a 3D setting $\mathcal{A} = \{\text{Ascend}, \text{Descend}, \text{Forward}, \text{TurnLeft}, \text{TurnRight}, \text{Done}\}$. In the AI2THOR simulator, *Ascend*, *Descend*, and *Forward* will move the aerial robot by 0.15 m. *TurnLeft* and *TurnRight* will rotate the agent by 30°. The *Done* action helps the agent

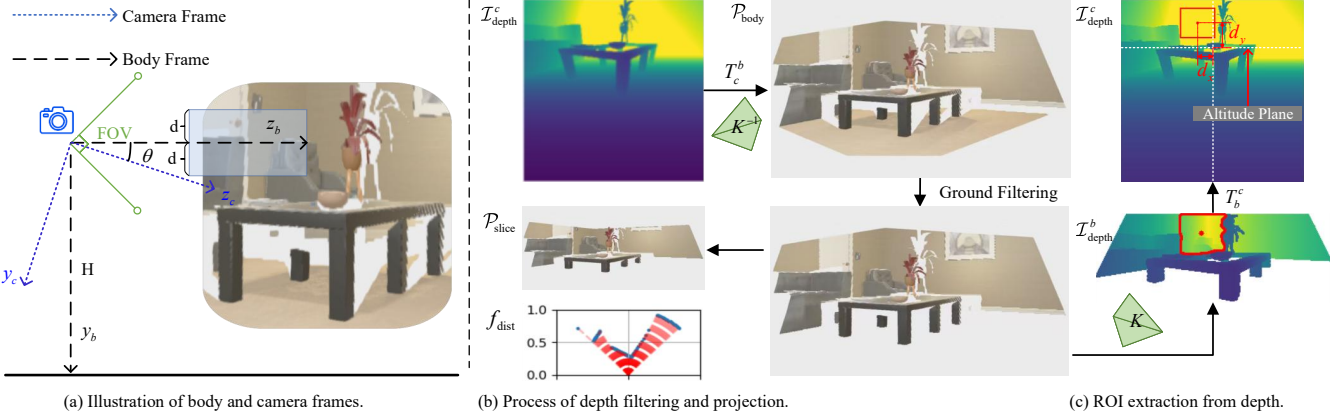


Fig. 3. Process of spatial perception from depth images.

learn to finish the task when the target object is close enough. The task is considered successful when 1) the bounding box center lies in the central 80% of the image; 2) the distance to the goal is less than 1.5 m; 3) the agent chooses *Done*.

B. Cross-Modality Attention

To enable zero-shot understanding of textual goals, CLIP [19] is used to ground vision with natural-language descriptions. Specifically, \mathcal{I}_{rgb} is partitioned into N patches $\{p_i\}_{i=1}^N$. Each patch is mapped to a visual embedding via the CLIP image encoder:

$$v_i = \text{CLIP}_{\text{image}}(p_i) \in \mathbb{R}^d. \quad (1)$$

Meanwhile, the CLIP text encoder generates the semantic embedding of the target object class c_t via

$$v_c = \text{CLIP}_{\text{text}}(c_t) \in \mathbb{R}^d. \quad (2)$$

The cosine similarity for each patch-text pair is computed as

$$s_i = \frac{v_i^\top v_c}{\|v_i\|_2 \|v_c\|_2} \in [-1, 1], \quad i = 1, \dots, N. \quad (3)$$

The resulting similarity map $f_{\text{semantic}} = [s_i]_{i=1}^N \in \mathbb{R}^N$ indicates which visual regions are most relevant to the target. The introduction of foundation models enables zero-shot ObjectNav by leveraging knowledge acquired from large-scale pretraining, without requiring any object-specific finetuning. Furthermore, the similarity map serves as an attention guide for the goal-reaching policy.

For perceptual information, we employ DINOv2 [28] to extract visual features and an object detector like YOLO [29] to obtain geometric cues from bounding boxes.

C. Spatial Perception From Depth

Depth information is essential for RL agents to perceive and reason about spatial structure. This section describes how depth images are leveraged to guide both obstacle avoidance and exploration, as is illustrated in Fig. 3.

1) *Depth Projection for Obstacle Avoidance*: To enhance spatial perception for navigation safety, the raw depth $\mathcal{I}_{\text{depth}}^c$ in the camera frame is projected onto the horizontal plane at the current flight altitude to obtain a 2D laser scan f_{dist} , which indicates the closest distance to obstacles, as illustrated in Fig. 3(b). Specifically, given the camera intrinsic matrix K , pixels with homogeneous coordinate $\tilde{p} = [u, v, 1]^\top$ and depth z can be back-projected to a 3D point cloud in the camera frame as

$$p_c = zK^{-1}\tilde{p} = [x_c, y_c, z_c]^\top. \quad (4)$$

The point cloud $\mathcal{P}_{\text{body}} = \{p_b\}$ in the body frame can be obtained by the homogeneous transformation of $\tilde{p}_c = [p_c^\top, 1]^\top$:

$$\tilde{p}_b = T_c^b \tilde{p}_c = [p_b^\top, 1]^\top = [x_b, y_b, z_b, 1]^\top. \quad (5)$$

where $T_c^b \in SE(3)$ is the extrinsic matrix from the camera frame to the body frame. We then apply a height filter on $\mathcal{P}_{\text{body}}$ to extract a horizontal slice after excluding the ground $\mathcal{P}_{\text{slice}} = \{p_b \in \mathcal{P}_{\text{body}} \mid -d \leq y_b \leq d\}$, as shown in Fig. 3(b). $\mathcal{P}_{\text{slice}}$ is then transformed from Cartesian to polar coordinates $\mathcal{P}_{\text{polar}} = \{(\rho, \phi) \mid \rho \in [0, 1], \phi \in [-\bar{\phi}, \bar{\phi}]\}$, where ρ and ϕ denote the normalized radial distance and azimuth angle, respectively. $\bar{\phi}$ is determined by the camera's horizontal field of view. $\mathcal{P}_{\text{polar}}$ can be uniformly divided into N sectors according to the range of ϕ , i.e., $\mathcal{P}_{\text{polar}} = \bigcup_{k=1}^N \mathcal{P}_{\text{polar}}^k$, where $\mathcal{P}_{\text{polar}}^k$ is defined as

$$\mathcal{P}_{\text{polar}}^k = \{(\rho, \phi) \in \mathcal{P}_{\text{polar}} \mid \phi \in [-\bar{\phi} + (k-1)\frac{2\bar{\phi}}{N}, -\bar{\phi} + k\frac{2\bar{\phi}}{N}]\}. \quad (6)$$

For each sector $\mathcal{P}_{\text{polar}}^k$, the closest distance to obstacles is

$$\rho_k^{\min} = \min_{(\rho, \phi) \in \mathcal{P}_{\text{polar}}^k} \rho. \quad (7)$$

Concatenating ρ_k^{\min} from the N sectors produces the 2D laser scan-like feature $f_{\text{dist}} = [\rho_1^{\min}, \dots, \rho_N^{\min}] \in \mathbb{R}^N$, which indicates the distribution of nearby obstacles.

2) *Depth ROI for Exploration*: Vision-based pose estimation is prone to drift, and a mapless exploration strategy can mitigate this issue by eliminating the need for explicit mapping. Inspired by [30] that guides indoor exploration by

visual cues, regions with larger depth values often indicate open and navigable space with increased probability of finding the target. To this end, the point cloud $\mathcal{P}_{\text{body}}$ from Eq. (5) is used to extract a Region of Interest (ROI) for visual tracking. As shown in Fig. 3(c), the ground in $\mathcal{P}_{\text{body}}$ is first filtered, and the remaining points are projected onto the image plane using the camera intrinsics K to obtain $\mathcal{I}_{\text{depth}}^b$. Then, the farthest valid regions are identified by thresholding the upper percentile of the depth values. Among these regions, the connected component with the largest area is selected as the ROI, from which the bounding box is extracted. Finally, the ROI feature f_{ROI} is presented as

$$f_{\text{ROI}} = [d_x, d_y, \bar{z}_{\text{ROI}}]^\top. \quad (8)$$

where $d_x, d_y \in [0, 1]$ represent the normalized offset of the box centroid from the origin of the current altitude plane, as illustrated in Fig. 3(c). \bar{z}_{ROI} denotes the mean depth of the ROI in $\mathcal{I}_{\text{depth}}^b$. In summary, the ROI feature f_{ROI} captures directional information from the agent to the ROI target, which is essential for the exploration policy.

D. Goal-Reaching Policy Training

On the iTHOR [11] benchmark, we extend the action space for 3D ObjectNav. Policies trained on iTHOR will be used solely for goal-reaching due to their limited exploration capability. The class set $C = \{S, U\}$, where S is defined as the seen class set during the policy training and U denotes the unseen set. In the training phase, the initial agent pose and the object class $c_t \in S$ are randomly selected at the beginning of each episode. In the testing phase, the target object class is chosen from $\{S, U\}$ to evaluate its generalization to unseen objects. Following previous works [7]–[9], RL training adopts parallel environments and Asynchronous Advantage Actor-Critic (A3C) [31] to enable efficient asynchronous learning and improve generalization across diverse scenarios. The key challenge lies in designing appropriate multi-modal inputs and reward functions to effectively guide the policy behavior, as described below.

1) Approaching Reward:

$$R_d = \|d_{t-1} - d_t\|_2, \quad (9)$$

where d_t denotes the distance to the closest target object at time t .

2) Parent Reward: Following MJO [5], the agent will receive a reward when it observes the target's parent object for the first time,

$$R_{\text{parent}} = \begin{cases} r_p, & \text{if target's parent is seen,} \\ 0, & \text{otherwise.} \end{cases} \quad (10)$$

It helps reduce exploration difficulty by guiding the agent toward reasonable regions that increase the likelihood of locating the target.

3) Bounding Box Reward: The bounding box of the target object is obtained either from the AI2THOR simulator or existing object detection algorithms. For the perceptual

module illustrated in Fig. 2, the feature f_{bbox} contains specific geometric cues of detected objects, defined as

$$f_{\text{bbox}} = [c_x, c_y, w, h, S_{\text{bbox}}/S_{\text{all}}, H] \quad (11)$$

where c_x, c_y are the normalized center coordinates of the bounding box, and w, h represent its normalized width and height. $S_{\text{bbox}}/S_{\text{all}}$ indicates the relative area of the object within the image. H corresponds to the current altitude. The bounding box reward is designed as

$$R_{\text{bbox}} = \min(S_{\text{bbox}}/S_{\text{all}}, 0.1), \quad (12)$$

which encourages the agent to approach the target. The final reward for goal-reaching is summarized as

$$r_g = R_d + R_{\text{parent}} + R_{\text{bbox}} + R_{\text{suc}} + R_c + \gamma, \quad (13)$$

where $R_{\text{suc}} = +5$ is the success reward, $\gamma = -0.02$, $R_c = -0.1$ are the step and collision penalty, respectively.

E. Exploration Policy Training

The iTHOR benchmark mainly includes single-room scenarios, where the agent can observe the target simply by flying higher and scanning the surroundings. Consequently, the trained goal-reaching policy exhibits limited exploration capability. To improve the exploration, we train an extra exploration policy on ProcTHOR [32], a more complicated benchmark featuring multi-room layouts. The exploration policy aims to approach the depth ROI in Fig. 3(c) while avoiding obstacles. The reward function that encourages exploration is designed as follows:

1) *Approaching Reward*: In Eq. (8), the mean depth of the ROI \bar{z}_{ROI} reflects whether the agent is moving closer to the ROI target. Thus, the approaching reward is defined as

$$R_{\text{forward}} = \min(\max(\bar{z}_{\text{ROI}}^{t+1} - \bar{z}_{\text{ROI}}^t, -0.2), 0.2). \quad (14)$$

2) *Direction Reward*: To move toward the right direction, the agent must learn how to correct its pose through turning maneuvers and vertical motions. In this case, the coordinates of the ROI centroid d_x, d_y in Eq. (8) provide crucial guidance for direction correction, leading to the direction reward

$$R_{\text{dir}} = \begin{cases} -0.75d, & d > d_{\text{thr}}, \\ 0, & d \leq d_{\text{thr}}, \end{cases}, d = \sqrt{d_x^2 + (2d_y)^2} \quad (15)$$

where the threshold $d_{\text{thr}} = 0.3$ helps avoid oscillatory behavior caused by frequent direction correction. The coefficient of d_y is set as 2 to enhance the sensitivity to height variations.

3) *Safety Reward*: For aerial robots, safety issues are critical in cluttered indoor environments. Obstacle avoidance relies heavily on the feature $f_{\text{dist}} = [\rho_1^{\min}, \dots, \rho_N^{\min}]$ from Eq. (7). We denote a safety distance by $\rho_{\min} = \min_{i=1:N} \rho_i^{\min}$. To encourage the agent to steer away from nearby obstacles, the safety reward is designed as

$$R_{\text{safe}} = \begin{cases} 1 - e^{2(\rho_{\text{thr}} - \rho_{\min})}, & \rho_{\min} \leq \rho_{\text{thr}}, \\ 0, & \rho_{\min} > \rho_{\text{thr}}, \end{cases} \quad (16)$$

where the safety threshold $\rho_{\text{thr}} = 1/3$ corresponds to a physical distance of 1 m in our experiments for a maximum

TABLE I
DETAILS OF SEEN/UNSEEN (S/U) OBJECT SPLITS.

Room	18/4 Split	14/8 Split
Kitchen	S: Spatula, Bread, Mug, CoffeeMachine, Apple U: Toaster	S: Spatula, Bread, Mug, CoffeeMachine U: Apple, Toaster
Living Room	S: Painting, Vase, RemoteControl, ArmChair, Television U: Laptop	S: Painting, Vase, RemoteControl, ArmChair U: Television, Laptop
Bedroom	S: Blinds, DeskLamp, Book, AlarmClock U: Pillow	S: Blinds, DeskLamp, Book U: AlarmClock, Pillow
Bathroom	S: SoapBar, Towel, SprayBottle, Mirror U: ToiletPaper	S: SoapBar, Towel, SprayBottle U: ToiletPaper, Mirror

depth range of 3 m . Finally, the reward for the exploration policy training is summarized as

$$r_e = R_{\text{forward}} + R_{\text{dir}} + R_{\text{safe}} + \gamma, \quad (17)$$

where $\gamma = -0.01$ is the step penalty.

IV. EXPERIMENTS

In this section, we conduct experiments to analyze the impact of multi-modal inputs and different rewards on indoor aerial ObjectNav. All algorithms are trained on the AI2THOR platform for a fair comparison. Four metrics are used to evaluate navigation performance: Success Rate (SR), Success weighted by Path Length (SPL), Collision Rate (CR), and Free-space Coverage Ratio (FCR).

A. Training and Evaluation Setup

The policy training needs online interaction with the AI2THOR simulator, where the iTHOR benchmark includes 120 realistic indoor scenarios, 80 rooms for training and 40 rooms for evaluation. As shown in Table I, there are 4 different types of room layouts: Kitchen, Living room, Bedroom, and Bathroom. Each kind of room contains different target object classes, divided into the seen and unseen sets. The goal-reaching policy AION-g and ObjectNav baselines are trained for 1×10^7 steps on iTHOR using two RTX 4090 GPUs, and then evaluated on the same test set used in [5]. Each room type is tested for 150 episodes.

Since iTHOR can not provide sufficient scene complexity to learn exploration behaviors, we train the exploration policy AION-e for 4×10^6 steps on ProcTHOR, which contains over 10,000 procedurally generated indoor scenes with substantially larger spatial scale and layout diversity.

B. Baseline Models for Goal-Reaching

On the iTHOR benchmark, we compare AION-g with state-of-the-art (SOTA) and open-source baselines that integrate exploration and goal-reaching. Since the baselines are originally designed for 2D ObjectNav, we extend their action space to 3D while keeping their original network structures.

All baselines are retrained from scratch in 3D ObjectNav tasks.

BaseModel [8] adopts convolutional neural networks to extract visual features from \mathcal{I}_{rgb} , and the target object class is encoded as a GloVe [33] embedding. All feature embeddings are concatenated as inputs to an LSTM-based actor-critic policy, which is trained by A3C.

Scene Prior [6] incorporates prior knowledge of scenes into the navigation policy using Graph Convolutional Networks (GCNs).

MJO [5] abandons visual backbones and only exploits hierarchical relationships for ObjectNav based on an object detector and GCNs. GloVe is used for text understanding.

SSNet [7] is an attention-based algorithm that guides the agent to search for objects with a high semantic similarity to the target. It supports zero-shot object navigation by computing a similarity map using GloVe.

C. Evaluation of Goal-Reaching Policy

Table II presents the comparison results of goal-reaching performance given seen/unseen objects. Since baseline models were originally designed for 2D ObjectNav, directly training them in 3D settings yields poor performance. According to the ablation study in Table III, where f_{bbox} plays a crucial role in improving navigation performance, we augment the original inputs of all baselines with feature f_{bbox} to ensure a fair comparison.

For both seen and unseen objects, AION-g achieves the best performance in SR and SPL while maintaining a relatively low CR. Among the baselines, MJO achieves almost the highest SR. An increase in SR often leads to a higher CR, as the agent tends to take greater risks to approach the goal aggressively. In contrast, AION-g outperforms MJO by (+7.5%/-4.3%) in SR and (+5.9%/-3.5%) in SPL on the 18/4 split, with a notably lower CR. A similar trend can be observed on the 14/8 split, where AION-g outperforms the baselines across nearly all metrics. Our model not only achieves strong generalization to unseen objects but also enhances safety, which is largely attributed to depth observations. The navigation trajectories of AION-g in four different types of rooms are visualized in Fig. 4, where the chosen action at each step is annotated.

D. Ablation Study on Goal-Reaching Policy

To further analyze the contributions of different rewards and input features to the goal-reaching performance, ablation experiments are conducted and summarized in Table III. Among the multi-modal inputs, removing f_{bbox} causes a dramatic drop in both SR and SPL, indicating that bounding box information is crucial for aerial ObjectNav. Regarding the reward design, canceling collision penalty R_c leads to a sharp increase in CR. The parent reward R_{parent} exhibits a limited contribution, as its removal does not noticeably affect performance metrics. Overall, the remaining components all contribute positively to navigation performance.

TABLE II
COMPARISON RESULTS OF ZERO-SHOT OBJECTNAV ON THE iTHOR BENCHMARK.

Model	Seen/Unseen split	Seen class			Unseen class		
		SR(%) \uparrow	SPL(%) \uparrow	CR(%) \downarrow	SR(%) \uparrow	SPL(%) \uparrow	CR(%) \downarrow
BaseModel [8](w/ f_{bbox})		76.7	39.9	5.5	81.5	36.4	2.3
Scene Prior [6](w/ f_{bbox})		74.3	42.1	5.5	83.7	41.9	5.4
MJO [5](w/ f_{bbox})	18/4	81.2	52.0	11.4	90.7	51.7	14.2
SSNet [7](w/ f_{bbox})		72.3	50.4	9.8	77.8	50.0	12.2
AION-g		88.7	57.9	5.6	95.0	55.2	7.6
BaseModel (w/ f_{bbox})		73.3	47.3	10.9	70.8	46.6	9.1
Scene Prior (w/ f_{bbox})		79.3	52.7	6.5	71.0	44.8	5.1
MJO (w/ f_{bbox})	14/8	78.8	43.6	10.9	83.0	45.6	11.7
SSNet (w/ f_{bbox})		79.2	44.3	6.8	81.8	46.4	4.5
AION-g		84.7	61.2	4.8	87.0	60.5	5.2

TABLE III

ABLATION STUDIES ON MULTI-MODAL INPUTS AND REWARD DESIGNS.

Model	18 Seen class			4 Unseen class		
	SR \uparrow	SPL \uparrow	CR \downarrow	SR \uparrow	SPL \uparrow	CR \downarrow
AION-g	88.7	57.9	5.6	95.0	55.2	7.6
Inputs	w/o $f_{semantic}$	81.8	49.2	6.1	88.5	44.6
	w/o f_{dist}	82.8	39.9	7.1	88.3	36.7
	w/o f_{bbox}	14.0	8.6	1.1	16.2	9.1
	w/o f_{rgb}	77.0	52.6	8.0	80.3	51.5
Reward	w/o R_{bbox}	83.3	48.0	5.1	92.3	49.8
	w/o R_d	77.5	33.9	4.2	86.7	33.4
	w/o R_{parent}	86.5	58.3	7.3	96.7	62.3
	w/o R_c	83.8	39.4	26.4	93.5	35.9
						34.0



Fig. 4. ObjectNav trajectories of AION-g across different iTHOR rooms.

V. EVALUATION ON DRONES IN ISAACSIM

To test the real-time performance of algorithms under realistic drone dynamics, we conduct further experiments using IsaacSim [34] with Pegasus [35]. IsaacSim is well-known for providing photo-realistic rendering and high-fidelity physics simulation, while Pegasus integrates the PX4 autopilot and

ROS2, allowing it to closely approximate real-world flight. As shown in Fig. 5, scenes are provided by OmniGibson [36] with three houses selected for drone experiments: *Chemistry*, *Beechwood*, and *Ihlen*.

In our experiments, discrete actions from RL policies are interpreted as velocity references for the PX4 autopilot to track. Specifically, *Ascend* and *Descend* correspond to vertical velocities of $\pm 0.15 \text{ m/s}$ along the *Z*-axis; *Forward* applies a forward velocity of 0.8 m/s ; and the angular velocity is $\pm 25 \text{ }^{\circ}/\text{s}$ for *TurnLeft* and *TurnRight*. The inference frequency of AION policies reaches about 2.7 Hz on the RTX 4080S GPU. Considering the latency of control response, each RL action is executed for a duration of 0.5 s.

A. Evaluation of Exploration Policy

To provide an intuitive illustration of the real-time performance, the exploration policy AION-e is directly evaluated on drones in IsaacSim, where two metrics are considered: CR and FCR. In each scene, the agent starts from the initial position and is allowed to explore the environment for 150 steps. AION-e is compared to ObjectNav baselines that integrate exploration and goal-reaching. To enforce exploration, the target object is set to a class that does not exist in the scene. The average performance over 5 episodes is summarized in Table IV. Although ObjectNav baselines introduced in Table II consider comprehensive skills, including exploration, goal-oriented navigation, and collision avoidance, they struggle to generalize to larger scenes and exhibit poor exploration performance. The exploration trajectories in *Beechwood* is visualized in Fig. 6, where goal-reaching policies tend to explore local areas when the target is invisible. In comparison, AION-e emphasizes exploration and safety during training, yielding a significantly higher FCR (+7.2% in *Chemistry*, +20.6% in *Beechwood*, and +51.9% in *Ihlen*) while maintaining a low CR.

B. Evaluation of Dual-Policy ObjectNav

The most effective strategy for aerial ObjectNav is to combine exploration and goal-reaching via policy switching. This section compares the dual-policy performance by pairing AION-e with different goal-reaching polices. To



Fig. 5. Placement of unseen objects at varying heights across different indoor environments in IsaacSim.

TABLE IV

COMPARISON OF EXPLORATION PERFORMANCE IN ISAACSIM.

Algorithm	Chemistry		Beechwood		Ihlen	
	FCR↑	CR↓	FCR↑	CR↓	FCR↑	CR↓
MJO	37.4	8.0	39.2	14.7	14.4	19.2
SSNet	34.3	5.3	40.0	0.0	13.9	1.5
AION-g	49.9	6.8	41.8	0.0	22.5	2.3
AION-e	57.1	2.4	62.4	0.3	74.4	0.0

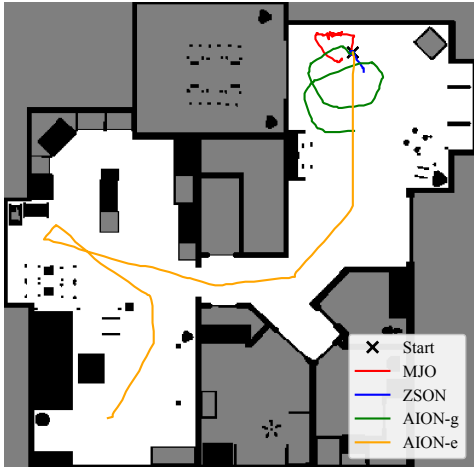


Fig. 6. Top-down view of 3D exploration trajectories in Beechwood.

evaluate zero-shot generalization, IsaacSim experiments use four unseen target objects during training. Average results over 5 episodes are reported in Table V, where dual-policy AION consistently attains the highest SR across all scenes. In most cases, CR is kept within a low range.

C. Failure Case Analysis

For goal-reaching performance, baseline methods often suffer from incorrect *Done* decisions or fail to approach the

TABLE V

OBJECTNAV PERFORMANCE ACROSS SCENES WITH UNSEEN OBJECTS IN ISAACSIM.

Algorithm	Objects	Chemistry		Beechwood		Ihlen	
		SR↑	CR↓	SR↑	CR↓	SR↑	CR↓
	Sofa	4/5	1.7	2/5	0.7	2/5	0.0
AION-e	Plant	2/5	1.2	4/5	1.2	3/5	0.0
& MJO	Laptop	0/5	1.1	3/5	7.2	5/5	0.4
	Microwave	2/5	0.0	4/5	6.6	2/5	2.3
	Sofa	0/5	2.4	1/5	2.1	2/5	0.0
AION-e	Plant	3/5	1.4	1/5	0.7	2/5	1.8
& SSNet	Laptop	0/5	0.7	3/5	2.2	2/5	0.0
	Microwave	1/5	4.4	4/5	1.0	3/5	1.3
	Sofa	4/5	1.0	5/5	1.7	4/5	1.5
AION-e	Plant	5/5	0.1	5/5	0.4	4/5	0.2
& AION-g	Laptop	2/5	0.7	5/5	1.6	5/5	0.0
	Microwave	3/5	0.0	5/5	1.8	5/5	0.8

target sufficiently. When the target is in the front, AION-g may occasionally prioritize goal-reaching while neglecting safety. In addition, since YOLOv8 is adopted as the object detector for all algorithms, misleading detection results constitute a primary cause of failure. In *Chemistry* of Table V, the dark environment severely degrades object detection and causes a low SR for the “Laptop” class. Regarding exploration performance, although AION-e improves search efficiency through specialized training, ensuring full coverage remains unsolved in the absence of a global map.

VI. CONCLUSIONS

In this paper, we present AION, a novel dual-policy RL framework for indoor aerial ObjectNav with 3D locomotion and zero-shot generalization. The design of multi-modal observations and reward functions is exploited to improve

both the exploration and goal-reaching performance. AION not only achieves SOTA results on iTHOR, but also validates its real-time performance under realistic drone dynamics. In summary, AION unlocks the potential of 3D ObjectNav in indoor environments and provides a practical solution for drone applications.

REFERENCES

- [1] T. Gervet, S. Chintala, D. Batra, J. Malik, and D. S. Chaplot, “Navigating to objects in the real world,” *Science Robotics*, vol. 8, no. 79, p. eadff6991, 2023.
- [2] M. Zhang, Y. Du, C. Wu, J. Zhou, Z. Qi, J. Ma, and B. Zhou, “Apex-nav: An adaptive exploration strategy for zero-shot object navigation with target-centric semantic fusion,” *arXiv preprint arXiv:2504.14478*, 2025.
- [3] K. Zhou, K. Zheng, C. Pryor, Y. Shen, H. Jin, L. Getoor, and X. E. Wang, “Esc: Exploration with soft commonsense constraints for zero-shot object navigation,” in *International Conference on Machine Learning*, 2023, pp. 42 829–42 842.
- [4] B. Yu, H. Kasaei, and M. Cao, “L3mvn: Leveraging large language models for visual target navigation,” in *2023 IEEE/RSJ International Conference on Intelligent Robots and Systems (IROS)*, 2023, pp. 3554–3560.
- [5] A. Pal, Y. Qiu, and H. Christensen, “Learning hierarchical relationships for object-goal navigation,” in *Conference on Robot Learning*, 2021, pp. 517–528.
- [6] W. Yang, X. Wang, A. Farhadi, A. Gupta, and R. Mottaghi, “Visual semantic navigation using scene priors,” *arXiv preprint arXiv:1810.06543*, 2018.
- [7] Q. Zhao, L. Zhang, B. He, H. Qiao, and Z. Liu, “Zero-shot object goal visual navigation,” in *2023 IEEE International Conference on Robotics and Automation (ICRA)*, 2023, pp. 2025–2031.
- [8] M. Wortsman, K. Ehsani, M. Rastegari, A. Farhadi, and R. Mottaghi, “Learning to learn how to learn: Self-adaptive visual navigation using meta-learning,” in *Proceedings of the IEEE/CVF conference on computer vision and pattern recognition*, 2019, pp. 6750–6759.
- [9] S. Lian and F. Zhang, “Tdanet: Target-directed attention network for object-goal visual navigation with zero-shot ability,” *IEEE Robotics and Automation Letters*, 2024.
- [10] X. Puig, E. Undersander, A. Szot, M. D. Cote, T. Yang, R. Partsey, R. Desai, A. Clegg, M. Hlavac, S. Y. Min, V. Vondrus, T. Gervet, V. Berges, J. M. Turner, O. Maksymets, Z. Kira, M. Kalakrishnan, J. Malik, D. S. Chaplot, U. Jain, D. Batra, A. Rai, and R. Mottaghi, “Habitat 3.0: A co-habitat for humans, avatars, and robots,” in *The Twelfth International Conference on Learning Representations, ICLR 2024, Vienna, Austria, May 7-11, 2024*, 2024.
- [11] E. Kolve, R. Mottaghi, W. Han, E. VanderBilt, L. Weihs, A. Herrasti, M. Deitke, K. Ehsani, D. Gordon, Y. Zhu, et al., “Ai2-thor: An interactive 3d environment for visual ai,” *arXiv preprint arXiv:1712.05474*, 2017.
- [12] H. Luo, A. Yue, Z.-W. Hong, and P. Agrawal, “Stubborn: A strong baseline for indoor object navigation,” in *2022 IEEE/RSJ International Conference on Intelligent Robots and Systems (IROS)*, 2022, pp. 3287–3293.
- [13] N. Yokoyama, S. Ha, D. Batra, J. Wang, and B. Bucher, “Vlfm: Vision-language frontier maps for zero-shot semantic navigation,” in *2024 IEEE International Conference on Robotics and Automation (ICRA)*, 2024, pp. 42–48.
- [14] D. S. Chaplot, D. P. Gandhi, A. Gupta, and R. R. Salakhutdinov, “Object goal navigation using goal-oriented semantic exploration,” *Advances in Neural Information Processing Systems*, vol. 33, pp. 4247–4258, 2020.
- [15] W. Cai, S. Huang, G. Cheng, Y. Long, P. Gao, C. Sun, and H. Dong, “Bridging zero-shot object navigation and foundation models through pixel-guided navigation skill,” in *2024 IEEE International Conference on Robotics and Automation (ICRA)*, 2024, pp. 5228–5234.
- [16] J. Peng, W. Cai, Y. Yang, T. Wang, Y. Shen, and J. Pang, “Logoplanner: Localization grounded navigation policy with metric-aware visual geometry,” *arXiv preprint arXiv:2512.19629*, 2025.
- [17] X. Sun, L. Liu, H. Zhi, R. Qiu, and J. Liang, “Prioritized semantic learning for zero-shot instance navigation,” in *European Conference on Computer Vision*, 2024, pp. 161–178.
- [18] H. Du, L. Li, Z. Huang, and X. Yu, “Object-goal visual navigation via effective exploration of relations among historical navigation states,” in *Proceedings of the IEEE/CVF Conference on Computer Vision and Pattern Recognition*, 2023, pp. 2563–2573.
- [19] A. Radford, J. W. Kim, C. Hallacy, A. Ramesh, G. Goh, S. Agarwal, G. Sastry, A. Askell, P. Mishkin, J. Clark, et al., “Learning transferable visual models from natural language supervision,” in *International conference on machine learning*, 2021, pp. 8748–8763.
- [20] J. Li, D. Li, S. Savarese, and S. Hoi, “Blip-2: Bootstrapping language-image pre-training with frozen image encoders and large language models,” in *International conference on machine learning*. PMLR, 2023, pp. 19 730–19 742.
- [21] R. Dang, L. Wang, Z. He, S. Su, J. Tang, C. Liu, and Q. Chen, “Search for or navigate to? dual adaptive thinking for object navigation,” in *Proceedings of the IEEE/CVF International Conference on Computer Vision*, 2023, pp. 8250–8259.
- [22] J. Lee, T. Miyanishi, S. Kurita, K. Sakamoto, D. Azuma, Y. Matsuo, and N. Inoue, “Citynav: A large-scale dataset for real-world aerial navigation,” in *Proceedings of the IEEE/CVF International Conference on Computer Vision*, 2025, pp. 5912–5922.
- [23] J. Xiao, Y. Sun, Y. Shao, B. Gan, R. Liu, Y. Wu, W. Guan, and X. Deng, “Uav-on: A benchmark for open-world object goal navigation with aerial agents,” in *Proceedings of the 33rd ACM International Conference on Multimedia*, 2025, pp. 13 023–13 029.
- [24] S. Liu, H. Zhang, Y. Qi, P. Wang, Y. Zhang, and Q. Wu, “Aerilavln: Vision-and-language navigation for uav,” in *Proceedings of the IEEE/CVF International Conference on Computer Vision*, 2023, pp. 15 384–15 394.
- [25] X. Wang, D. Yang, Y. Liao, W. Zheng, B. Dai, H. Li, S. Liu, et al., “Uav-flow colosse: A real-world benchmark for flying-on-a-word uav imitation learning,” *arXiv preprint arXiv:2505.15725*, 2025.
- [26] X. Liu, Y. Liu, H. Qiu, Y. Qirong, and Z. Lian, “Indooruav: Benchmarking vision-language uav navigation in continuous indoor environments,” *arXiv preprint arXiv:2512.19024*, 2025.
- [27] C. Huang, O. Mees, A. Zeng, and W. Burgard, “Visual language maps for robot navigation,” in *IEEE International Conference on Robotics and Automation, ICRA 2023, London, UK, May 29 - June 2, 2023*. IEEE, 2023, pp. 10 608–10 615.
- [28] M. Oquab, T. Daretz, T. Moutakanni, H. Vo, M. Szafraniec, V. Khalidov, P. Fernandez, D. Haziza, F. Massa, A. El-Nouby, et al., “Dinov2: Learning robust visual features without supervision,” *arXiv preprint arXiv:2304.07193*, 2023.
- [29] J. Redmon, S. Divvala, R. Girshick, and A. Farhadi, “You only look once: Unified, real-time object detection,” in *Proceedings of the IEEE conference on computer vision and pattern recognition*, 2016, pp. 779–788.
- [30] B. Sun, H. Chen, S. Leutenegger, C. Cadena, M. Pollefeys, and H. Blum, “Frontiernet: Learning visual cues to explore,” *IEEE Robotics and Automation Letters*, 2025.
- [31] V. Mnih, A. P. Badia, M. Mirza, A. Graves, T. Lillicrap, T. Harley, D. Silver, and K. Kavukcuoglu, “Asynchronous methods for deep reinforcement learning,” in *International conference on machine learning*, 2016, pp. 1928–1937.
- [32] M. Deitke, E. VanderBilt, A. Herrasti, L. Weihs, J. Salvador, K. Ehsani, W. Han, E. Kolve, A. Farhadi, A. Kembhavi, and R. Mottaghi, “ProcTHOR: Large-Scale Embodied AI Using Procedural Generation,” in *NeurIPS*, 2022, outstanding Paper Award.
- [33] J. Pennington, R. Socher, and C. D. Manning, “Glove: Global vectors for word representation,” in *Proceedings of the 2014 conference on empirical methods in natural language processing (EMNLP)*, 2014, pp. 1532–1543.
- [34] NVIDIA, “Isaac Sim.” [Online]. Available: <https://github.com/isaac-sim/IsaacSim>
- [35] M. Jacinto, J. Pinto, J. Patrikar, J. Keller, R. Cunha, S. Scherer, and A. Pascoal, “Pegasus simulator: An isaac sim framework for multiple aerial vehicles simulation,” in *2024 International Conference on Unmanned Aircraft Systems (ICUAS)*, 2024, pp. 917–922.
- [36] C. Li, R. Zhang, J. Wong, C. Gokmen, S. Srivastava, R. Martín-Martín, C. Wang, G. Levine, M. Lingelbach, J. Sun, et al., “Behavior-1k: A benchmark for embodied ai with 1,000 everyday activities and realistic simulation,” in *Conference on Robot Learning*, 2023, pp. 80–93.